Journal of Nuclear Medicine, published on February 9, 2017 as doi:10.2967/jnumed.116.188649

Multiparametric imaging of tumor hypoxia and perfusion with ^{18}F-FMISO dynamic PET in head and neck cancer

Milan Grkovski[1], Heiko Schöder[2], Nancy Y. Lee[3], Sean D. Carlin[2], Bradley J. Beattie[1], Nadeem Riaz[3], Jonathan E. Leeman[3], Joseph A. O'Donoghue[1] and John L. Humm[1]

[1]Department of Medical Physics, Memorial Sloan Kettering Cancer Center, New York, New York

[2]Department of Radiology, Memorial Sloan Kettering Cancer Center, New York, New York

[3]Department of Radiation Oncology, Memorial Sloan Kettering Cancer Center, New York, New York

Running title: Multiparametric imaging with FMISO PET

Keywords: ^{18}F-fluoromisonidazole; FMISO; hypoxia; perfusion; dynamic PET; head and neck cancer;

Financial support: This study was supported by National Institutes of Health grants 5R01CA157770-04 (P.I. Nancy Y. Lee), U01 CA157442-3 (P.I. Sadek A. Nehmeh) and the cancer center grant P30 CA008748 (P.I. Craig B. Thompson).

Corresponding Author:

Milan Grkovski, PhD
Department of Medical Physics
Memorial Sloan Kettering Cancer Center
1275 York Avenue
New York, NY 10065
Phone: 212-639-2480
Email: grkovskm@mkscc.org

Conflict of Interest: The authors declare no potential conflicts of interest.

Word count: 5537

Figures: 6
Tables: 4

Abstract

Tumor hypoxia and perfusion are independent prognostic indicators of patient outcome. We developed the methodology for, and investigated the utility of multiparametric imaging of tumor hypoxia and perfusion with ^{18}F-fluoromisonidazole (FMISO) dynamic positron emission tomography (dPET) in head and neck cancer (HNC).

Methods: 120 HNC patients underwent 0-30 min FMISO dPET in a customized immobilization mask, followed by 10 min static acquisitions starting at 93±6 and 160±13 min post-injection. A total of 248 lesions (≥2 cm^3) were analyzed. Voxelwise pharmacokinetic modeling was conducted using an irreversible one-plasma two-tissue compartment model to calculate surrogate biomarkers of tumor hypoxia (k_3), perfusion (K_1) and FMISO distribution volume (DV). The analysis was repeated with truncated dPET datasets.

Results: Substantial inter- and intra-tumor heterogeneity was observed for all investigated metrics. Equilibration between the blood and unbound FMISO was rapid in all tumors. FMISO distribution volume deviated from the expected value of unity, causing discrepancy between k_3 maps and total FMISO uptake, and reducing the dynamic range of total FMISO uptake for quantifying the degree of hypoxia. Both positive and negative trends between hypoxia and perfusion were observed in individual lesions. All investigated metrics were reproducible when calculated from truncated 20-min dataset.

Conclusion: FMISO dPET provides the data necessary to generate parametric maps of tumor hypoxia, perfusion and radiotracer distribution volume. These data clarify the ambiguity in interpreting FMISO uptake and improve the characterization of lesions. We show total acquisition times can be reduced to 20-min, facilitating the translation of FMISO dPET into the clinic.

Introduction

The presence of hypoxia is a common feature of solid tumors including head and neck cancer (HNC; ref. 1). In cancer, hypoxia is a pivotal factor that influences the effectiveness of radiation, chemo, and immune therapies (2, 3). It promotes angiogenesis (4), genomic instability and tumor metastasis (5), and is associated with poor overall survival (6, 7).

Non-invasive quantitative imaging of tumor hypoxia with ^{18}F-fluoromisonidazole (FMISO) positron emission tomography (PET) is clinically feasible (8, 9) and reproducible (10, 11). FMISO uptake has been reported to be an independent prognostic biomarker in HNC patients in both retrospective (1) and prospective (12) studies. PET is the preferred method of evaluating tumor hypoxia due to its high specificity and sensitivity, and FMISO continues to be the most extensively studied hypoxia radiotracer (13). The predominant practice consists of a single static PET acquisition at 2-4 hr post injection, with a target-to-blood ratio (*TBR*) of 1.2-1.4 typically being the hypoxia defining threshold (1, 8, 9).

The validity of a threshold-based approach relies on two implicit assumptions: (i) FMISO equilibration is sufficiently fast that at the time of imaging the concentration of unbound FMISO in the tissue has reached a fixed ratio relative to that in the blood, and (ii) that this ratio, also known as the distribution volume (*DV*) is the same across all tissues, including tumors. Patlak and Blasberg demonstrated that once equilibration is achieved, *DV* becomes the threshold above which any accumulation of tracer is due to irreversible binding (14). The use of *TBR* thresholds assumes that all tissues have a *DV* of ~1.0, and incorporates a margin of error to avoid misidentification of hypoxia due to image noise. However, if the foregoing assumptions are invalid, a threshold-based metric will not reflect the underlying hypoxia status directly.

In addition, late static scans do not provide information on tumor perfusion that may be important in distinguishing tumor subtypes with different diagnostic and therapeutic requirements (15). As FMISO passively and rapidly diffuses out of the vasculature and through cell membranes due to its lipophilicity (octanol-water partition coefficient of ~0.4; ref. 13), its regional uptake at initial times post-injection is

expected to reflect tissue perfusion (16). A complex relationship between tumor hypoxia, perfusion and glucose metabolism supports the use of composite metrics that offer additional information on tumor adaptation to the microenvironment (17, 18) and may be better predictors of overall survival (19, 20). However, protocols incorporating several PET radiotracers administered in multiple imaging sessions can become overly complex and may be restricted by regulatory limits on ionizing radiation exposure (21). Moreover, despite reports that pharmacokinetic model-based metrics derived from FMISO or ^{18}F-fluorodeoxyglucose (FDG) dPET studies confer advantage over static uptake-based indices (19, 22-24), dynamic PET protocols have not yet been widely adopted, in part due to their clinical impracticality.

In the current study, 120 head and neck cancer patients underwent simultaneous multiparametric imaging of tumor hypoxia and perfusion with FMISO dPET. We hypothesized that (i) pharmacokinetic modeling of FMISO dPET reveals additional layers of inter- and intra-tumor heterogeneity and helps interpret static FMISO images, and (ii) FMISO dPET can be performed with acquisition times comparable to whole body FDG PET while maintaining a high degree of accuracy and precision.

Materials and Methods

Patient selection

This retrospective pilot study was approved by Memorial Sloan Kettering Cancer Center's Institutional Review Board (Protocol 04-070; registered under www.clinicaltrials.gov identifier NCT00606294) and all subjects signed a written informed consent regarding the examination and use of anonymous data for research and publication purposes. The methods were carried out in accordance with the approved guidelines. Patients aged 18+ years with a histologically confirmed diagnosis of squamous cell carcinoma of the head and neck and Karnofsky performance status of ≥70 were eligible. Exclusion criteria included all nasopharyngeal, paranasal sinus, salivary cancer and thyroid malignancies, prior chemotherapy or radiotherapy within the last three years, previous surgical resection for the same disease, any prior radiotherapy to the head and neck region, and pregnancy.

120 patients, aged 59±10 years (range, 25-86 years) were included in the study between January 2011 and August 2016 (Table 1). Patients were screened for their human papillomavirus (HPV; by in situ hybridization) and p16 status (by immunohistochemistry), prognostic indicators in HNC (25). All patients were scanned on a flat-top couch wearing a customized radiotherapy treatment immobilization mask that minimizes motion and allows for accurate repositioning. Intravenous lines inserted in antecubital veins were used for radiotracer injection.

PET/CT imaging

All patients received baseline FDG PET/CT scans of the head and neck, followed by baseline FMISO dynamic PET/CT scans 9±7 days thereafter. No interventions were performed between FDG and FMISO PET/CT scans. The FDG scans consisted of a 465±12 MBq injection of FDG, administered after a fasting period of ≥6 hours. The PET acquisition commenced at 76±12 min post-injection on General Electric Discovery ST PET/CT (GE Health Care Inc.) using two bed positions each lasting 5 minutes. The x-ray computed tomography (CT) images acquired immediately prior to this used the following settings: 140 kVp, 250 mAs, and 3.8-mm slice thickness.

Dynamic FMISO PET/CT scans (FMISO1) at a single bed position were performed on either Discovery STE PET/CT or 710 PET/CT in time-of-flight mode. FMISO was prepared as described previously (26). The dynamic PET acquisition was initiated concurrent to the intravenous bolus injection of 389±15 MBq of FMISO. Data were acquired for 30 min and binned into 6×5-sec, 3×10-sec, 4×60-sec, 2×150-sec, and 2×300-sec frames. Two additional 10-min static image sets, FMISO2 starting at 93±6 min and FMISO3 starting at 160±13 min post-injection were also acquired. Patients rested in quiet waiting rooms between scans. Prior to each FMISO PET scan, a low-dose CT scan was performed for attenuation correction and image registration purposes (120 kVp, 3.8-mm slice thickness, and 40 mAs, 10 mAs, and 80 mAs for the first, second and third scans, respectively).

All PET emission data was corrected for attenuation, scatter, and random events, and then iteratively reconstructed into a 256×256×47 matrix (voxel dimensions: 1.95×1.95×3.27 mm^3) using the ordered subset expectation maximization algorithm provided by the manufacturer (2 iterations, 20 subsets for DST and DSTE scanners, 16 subsets incorporating time-of-flight and point spread function modeling for the D710 scanner, and a Gaussian post-filter of 6.4-mm full width at half maximum).

Image analysis

All three segments of the FMISO scan were spatially co-registered using the rigid-body transformation calculated with General Co-Registration™ tool (General Electric Advantage Workstation v4.7) applied to their corresponding CT scans to form a concatenated FMISO dPET scan. The FDG PET was co-registered to FMISO dPET using the respective CT images by the same technique. Lesions were delineated on the FDG PET images, using the adaptive threshold algorithm in the PET VCAR™ (Volume Computer Assisted Reading; General Electric Advantage Workstation v4.7) semi-automated software, based on the companion CT as a fiduciary marker and a count-based edge recognition algorithm.

Pharmacokinetic modeling

Pharmacokinetic modeling of FMISO dPET images was carried out in PMOD v3.604 (PMOD Technologies GmbH), utilizing an irreversible one-plasma two-tissue compartment model, in which the total concentration of activity measured by the PET scanner as a function of time *t* post-injection, *C(t)*, is given by

$$C(t) = v_B C_p(t) + (1 - v_B)\big(C_1(t) + C_2(t)\big), \quad (1)$$

where v_B is the fractional vascular volume, $C_p(t)$ is the activity concentration in the plasma, $C_1(t)$ is that of unbound activity in tissue, and $C_2(t)$ is that of the irreversibly bound hypoxia-localized radiotracer. C_1 and C_2 are calculated as

$$C_1(t) = K_1 e^{-(k_2+k_3)t} * C_p(t), \quad (2)$$

$$C_2(t) = \frac{K_1 k_3}{k_2+k_3}\left[1 - e^{(k_2+k_3)t}\right] * C_p(t), \quad (3)$$

where $*$ denotes convolution. By fitting the model to the data, three kinetic rate constants are derived: K_1, describing transport from the vascular compartment C_p to the extravascular tissue compartment C_1 (highly perfusion dependent and therefore used as a surrogate for local tumor perfusion); k_2, describing the transport of FMISO from the extravascular tissue compartment back to blood, and k_3, describing the rate of irreversible binding of FMISO within tumor compartment C_2 (a surrogate for hypoxia-mediated entrapment). A composite parameter DV representing the total FMISO distribution volume (i.e. overall concentration of unbound FMISO relative to blood) was also derived,

$$DV = v_B + (1 - v_B)\frac{K_1}{k_2}. \quad (4)$$

While v_B and DV are unitless, K_1 (assuming unit density tissue), k_2 and k_3 are expressed in min^{-1}. FMISO equilibration time, T^*, was calculated as

$$T^* = 7 \cdot \frac{\ln(2)}{(k_2+k_3)} \quad (5)$$

and represents the time after which unbound FMISO has reached >99% of its final ratio relative to blood.

To avoid invasive blood sampling, the input function (IF) was derived from the dynamic PET images, segmenting the ipsilateral (with respect to the lesion) jugular vein on the early frame with the highest image intensity (by selecting ~100 hottest voxels). IF time activity curves (TACs) were defined using the available temporal data and fitted with a triphasic exponential function, to obtain a modeled IF as

$$IF(t) = \begin{cases} Linear\ interpolation & t < t_0 \\ \sum_{i=1}^{3} A_i e^{-(t-t_0)\ln 2/T_i} & t \geq t_0 \end{cases}, \quad (6)$$

where IF(t) is the modeled activity concentration in the blood at time t, A_i and T_i terms represent the fitting parameters (Levenberg-Marquardt optimization, 50 random fits, 200 iterations), and t_0 defines at what time the model switches from linear to tri-exponential interpolation between measured values.

Partial volume correction was performed in PMOD as previously described, with correction factors converging towards 1 at late time points in all cases (27). Calculation of kinetic rate constants on a voxel-level was performed using the two-tissue compartment model with ridge-regression fitting as implemented in the PXMOD tool. *TBR* was derived from the FMISO3, using the measured activity concentration in the IF volume of interest (VOI), $C_p(t)$ as the reference,

$$TBR = \frac{C_{target}(t)}{C_p(t)}. \quad (7)$$

For radiotracers with irreversible trapping such as FMISO, *TBR* can be expressed via the standard Patlak formulation (13), which for $t>T^*$ becomes linear with the form:

$$TBR = \frac{K_1 k_3}{k_2+k_3} \cdot \frac{\int_0^t C_p(\tau)d\tau}{C_p(t)} + DV. \quad (8)$$

Note that due to its dependence on K_1, k_2, C_p and DV in addition to k_3, *TBR* in principle reflects hypoxic status less directly than k_3, which depends solely on hypoxia-mediated entrapment.

Pharmacokinetic modeling was also performed for normal tissues in the head and neck region, including sternocleidomastoid muscle, adipose tissue posterior to the cervical vertebrae and submandibular and parotid glands. For this purpose, VOIs were manually drawn on the CT image, and copied to the corresponding dPET dataset to derive the time activity curves. Kinetic rate constants were then calculated for each structure by fitting VOI-derived TACs.

To investigate the feasibility of utilizing shorter PET acquisition times, pharmacokinetic modeling for all intratumor voxels was repeated for truncated 20-min dynamic datasets that consist of first 10-min of FMISO1 and FMISO3 (the acquisition segment from ~160-170 min post injection). Input functions were derived from available temporal data. All metrics as calculated with truncated dataset (TD) were compared to those derived from full dataset (FD).

Statistical Analysis

The correlation strength between different indices was analyzed using Pearson's *r*. Comparisons of metrics from HPV and p16 positive/negative groups was performed with unpaired 2-tailed Student *t* test. $p<0.05$ was assumed to represent statistical significance. Regression analysis was performed to calculate slope and intercept coefficients (measure of correlation direction) together with 95% confidence intervals (CI). The root-mean-square deviation (RMSD) of the residuals for intratumor voxelwise measurements of all kinetic rate constants derived from FD and TD was calculated for each lesion (measure of reproducibility). Bland-Altman analysis was performed on pooled data to estimate the mean difference between parameters as calculated with TD and FD (measure of accuracy) and 95% limits of agreement (measure of precision).

Results

Kinetic rate constants and FMISO uptake for tumor and normal tissue

In total, 248 FDG-avid lesions were included in the analysis, ranging from 2-121 cm^3. For every intratumor voxel, both *TBR* and a full set of model parameter values were determined, summarized in Table 2. Also included are the corresponding values for sternocleidomastoid muscle, adipose tissue, submandibular gland and parotid gland. For all normal tissues, k_3 was close to zero, indicating insignificant levels of FMISO entrapment. *DV* and *TBR* were close to 1.0 in sternocleidomastoid muscle, submandibular and parotid glands. However, in adipose tissue both *DV* and consequently *TBR* were much lower. None of the foregoing metrics were significantly different between HPV positive (n=73) and HPV negative (n=15), or between p16 positive (n=96) and p16 negative (n=9) groups.

Relationships between target-to-blood ratio (*TBR*), hypoxia (k_3), perfusion (K_1) and FMISO distribution volume (*DV*)

Sagittal cross-sections through parametric images of *TBR*, k_3, K_1 and *DV* for 4 patient tumors highlight the intra- and inter-tumor heterogeneity and the different spatial relationships that may occur between the variables (Fig. 1). Line profiles through parametric maps of patient tumor #1 (Fig. 2A) indicate that towards the tumor center, k_3 continues to rise past the point of maximum *TBR* (which decreases due to decreasing *DV*), indicating a greater dynamic range of k_3 compared to the dynamic range of *TBR* for the purpose of quantifying the degree of hypoxia. The variation in *DV* broadens the voxelwise k_3-*TBR* scatterplot for this tumor so that a particular value of *TBR* can be associated with a wide range of k_3 values (Fig. 2B).

Patient tumor #2 represents a case where there is a more pronounced contradiction between the k_3 and *TBR* distributions. Time activity curves corresponding to two individual voxels (identified as #1 and #2) are presented in Fig. 2C. FMISO uptake in voxel #1 is initially high and rapidly diminishes, converging towards the input function TAC but eventually rising above it due to non-zero k_3. Voxel #2 exhibits initially low uptake that slowly increases with time but remains relatively low on the *TBR* image; however it appears more hypoxic on the k_3 image. The observed discrepancy is not caused by a continuing slow

washout of a high initial uptake in voxel #1 (T^* was <30 min in both cases). Rather, it is a direct consequence of the difference in *DV* (1.03 and 0.36 for voxels #1 and #2, respectively).

Visualizing *TBR* as a function of time after injection for patient tumor #3 reveals rapid accumulation of FMISO both in the lesion as well as in the submandibular and parotid glands, reaching *TBR*>1.3 after ~3-4 minutes post-injection. However, while FMISO gradually clears from the salivary glands, in the lesion it remains high, indicating a uniformly high distribution volume (Fig. 2D).

Both patient tumors #3 and #4 exhibit apparent agreement between *TBR* and k_3. However, for patient tumor #3, the intratumor hypoxic regions were positively correlated with the degree of perfusion, whereas for patient tumor #4 these were negatively correlated (Fig. 2E). Nevertheless, hypoxia (k_3) and perfusion (K_1) are largely independent at the population level, underscoring the fact that inverse K_1 parametric maps are not equivalent to an image of tumor hypoxia. Correlations between all investigated metrics are reported in Figure 3.

Population-based comparison of k_3 and *TBR*

Pearson's *r* between mean voxelwise k_3 and *TBR* from all 248 lesions was 0.73 (95% CI: 0.67-0.78; Fig. 4A). The scatterplot is color coded to display the mean voxelwise *DV* for each tumor. Substantial variation in *DV* across lesions reduces the k_3-*TBR* correlation over the patient population. For example, lesions #1 and #2 (Fig. 4A) have similar k_3 (0.0068 min^{-1} and 0.0074 min^{-1} respectively), but their *TBR*s are markedly different due to different *DV*s (*TBR*=2.49; *DV*=1.24 and *TBR*=1.08; *DV*=0.59 respectively). Consider also lesion #3 which has an identical *TBR (*1.08) to lesion #2, but has a *DV*=1.09 and is normoxic (k_3=0.0000 min^{-1}).

The analogous scatterplot for the pooled voxelwise data is presented in Fig. 4B (*r* = 0.74), with superimposed nominal hypoxia thresholds based on *TBR*=1.4 and the regression-equivalent k_3=0.0031 min^{-1}. These thresholds split the plane into four quadrants where the 1st and 3rd quadrants contain voxels that would be classified identically by both *TBR* and k_3 criteria; the 2nd and 4th quadrants contain voxels where the criteria disagree. The mean *DV* for voxels in the 1st, 2nd, 3rd and 4th quadrants are 0.98±0.16,

1.12±0.10, 0.98±0.15 and 0.72±0.16, respectively. Together, the 2nd and 4th quadrants contain approximately 25% of all tumor voxels.

Population Distributions of FMISO equilibration time and distribution volume

*T** was <90 min in >99% of tumor voxels (Fig. 5A). This could be construed as *prima facie* evidence for the use of static FMISO PET imaging in HNC at times greater than 90 min post injection. However, although the mean *DV* of 0.96±0.18 was indistinguishable from 1.0, the distribution is skewed towards lower values (skewness of 3.56) with 17% of all voxels having *DV*<0.8 and 8% with *DV*>1.2 (Fig. 5B).

FMISO dynamic PET with truncated acquisition protocols

Scatter plots and intensity histograms from pooled data are given for k_3 and K_1 as calculated with either FD or TD (Fig. 6A). Also displayed are k_3 and K_1 parametric maps as calculated with FD and TD, as well as their respective difference map (Fig. 6B), for the patient examples #1-4 presented in Figure 1. The reproducibility of all kinetic rate constants is summarized in Table 3. High degree of correlation was observed across a broad range of values when calculated using the truncated dataset, both from whole-tumor and voxelwise data (r≥0.98). High reproducibility of k_3 and K_1 on a lesion-by-lesion basis was indicated by low RMSD values. For pooled data, low mean differences indicate relatively high accuracy in the estimates, whereas narrow 95% limits of agreement on the mean differences indicate high precision.

The analysis was repeated for truncated datasets consisting of 15-min total acquisition time (5-min + 10-min). The results were more variable, with lower accuracy and precision of the parameter estimates (Table 4) due to the insufficient temporal information and resulting inadequate fitting of the input function.

Discussion

The importance of establishing a quantitative measure of tumor hypoxia derives from its potential clinical relevance as an imaging biomarker. Hypoxia has been shown to be a prognostic indicator of treatment outcome for a wide range of malignancies, including head and neck cancer (1, 7). This has fueled considerable interest in the use of PET radiotracers such as FMISO, where tumor hypoxia levels in patients can be measured non-invasively, quantitatively, and with high specificity and sensitivity. In the current study of 120 patients, we performed multiparametric imaging of tumor hypoxia as well as tumor perfusion, itself an independent prognostic indicator of treatment outcome (18, 19). Our results demonstrate: (i) the rate of FMISO equilibration is sufficiently fast in head and neck tumors to allow for late static imaging as a means of measuring hypoxia but this is thwarted by the substantial variability of *DV*; (ii) due to its dependence on non-uniform *DV*, *TBR* reflects hypoxic status of tumors less directly than k_3 and has a lower dynamic range, (iii) simultaneous measurement of hypoxia and perfusion reveals substantial intra- and inter-tumor heterogeneity, contributing invaluable information for phenotypic characterization of lesions; and (iv) FMISO dPET can be performed with short (20-min) composite imaging protocols while maintaining accuracy and precision in parameter estimation.

The widespread application of *TBR* threshold values is a consequence of the simplicity of static PET image acquisition and analysis. The validity of threshold-based definition of hypoxia is predicated upon the assumption of a uniform *DV* with a mean of 1.0 and dispersion not greater than what can be attributed to image noise. The observed wide distribution of *DV* at the intratumor voxel level results in either over- or underestimation of the degree of hypoxia. While it can partially be explained by statistical fluctuations, the root cause of this variability is currently unknown. *DV*<1.0 could represent voxels with aberrant composition of soluble and insoluble components within the tumor microenvironment or necrotic microregions with limited perfusion. On the other hand, intratumor voxels of patient tumor #3 had *DV* consistently higher than 1.0 (Fig. 2D). Other than hypoxia driven irreversible binding to intracellular macromolecules we are unaware of any process by which FMISO would concentrate in tumor tissue to explain this observation. Speculative mechanisms may include some degree of facilitated transmembrane transport in cells within tumors, local capillary tortuosity leading to elevated temporary non-specific accumulation in regions lacking functional lymphatics, or sub-voxel sized cyst or gland-like regions that

accumulate radiotracer at higher levels than blood. Variable inter-vessel distances within the tumor may be an additional factor that impacts the measured *DV* values, particularly if drug consumption is diffusion-limited. Also, the density of the metabolizing cells and levels of cellular nitroreductase may vary significantly. Due to its dependence on non-uniform *DV*, *TBR* is in principle a less direct biomarker of hypoxia-mediated accumulation of FMISO than k_3. Moreover, *TBR* also depends on imaging time post injection, whereas k_3 and *DV* are time independent metrics.

Imaging surrogates of tumor perfusion are clinically relevant as a way to measure the delivery of drugs to the tumor (28, 29). Several PET studies have reported the benefit of assessing tumor perfusion and hypoxia as predictors of response to therapy (20, 23, 24, 30, 31). These metrics may provide potentially valuable information for tumor characterization, treatment selection and monitoring response. For example, hypoxia-activated prodrugs or anti-angiogenic agents could be applied in cases of diffuse hypoxia with high perfusion, whereas patients presenting with a more focal hypoxia combined with very low perfusion may potentially benefit more from dose escalation to the tumor subvolume. Positive as well as negative correlations were found between k_3 and K_1. A negative trend supports the classical hypothesis that hypoxia develops in hypo-perfused tumor subvolumes with chaotic and dysfunctional microvasculature. Here the hypothetical mechanism is related to increased distances between functional capillary vasculature and tumor cells, such that distal cells receive less oxygen leading to diffusion-limited hypoxia. A positive correlation however supports previous observations that hypoxia may be present in well-perfused regions (32). This may reflect different types of hypoxia characterized in HNC tumors by Ljungkvist and colleagues (patchy, ribbon-like, and mixed), who demonstrated that, at the microscopic level, hypoxia and perfusion can coexist in close proximity (33). Here, hypoxia may drive angiogenesis, hyperperfusion and perfusion heterogeneity (4). Such regions could remain hypoxic due to low oxygen extraction ratio or high oxygen consumption rate. Heterogeneous mixture of vessels with fluctuating hemodynamics can induce longitudinal gradients, resulting in the delivery of either hypoxic or aerobic blood depending on the distance from the nearest arterial source (15). Other biologic explanations have been proposed to describe the presence of hypoxia in well-perfused tumor regions (34, 35). These hypothetical mechanisms are of interest in that they may represent a diversity of tumor phenotypes with

different biological, clinical and prognostic features. Only by multiparametric imaging can such subtle but potentially significant phenotypic discrimination be achieved non-invasively.

Despite the potential benefits of pharmacokinetic modeling, the long image acquisition protocols constitute a significant obstacle towards wider adoption of FMISO dynamic PET in clinical practice. We show that surrogate biomarkers of hypoxia and perfusion can be estimated accurately and precisely from 20-min truncated FMISO dynamic PET scans, albeit in one early and one late 10-min acquisition. As FMISO is relatively freely and rapidly diffusible, an initial 10-min dynamic acquisition is sufficient for the calculation of K_1. Overall shape of the input function can be approximated from the truncated dataset, facilitating the calculation of k_3. As a late 10-min acquisition remains part of the truncated dataset, the conventional static image evaluation of hypoxia can still be made.

Our study has some limitations. The majority of patients presented with HPV positive tumors; a good prognostic indicator associated with better 3-year rates of overall survival than patients with HPV-negative tumors (25). Only 3 out of 120 patients were deceased at the time of writing (median follow-up period: 20 months, range: 1-68 months), therefore survival analysis is presently underpowered due to a paucity of events. Co-registration of one FDG and three FMISO scans potentially resulted in small misalignments and changes in tumor size and shape may have occurred during the 9±7 day interval between the treatment planning FDG PET and FMISO PET scans. However, all patients were scanned in customized immobilization masks, increasing positioning accuracy and minimizing mismatches. All FDG-derived volumes of interest were visually inspected on FMISO PET/CT scans and no obvious mismatches or changes in tumor size were identified. While the current pipeline did not allow for full automation, it is likely that dedicated kinetic modeling software can simplify and expedite the analysis significantly, as all steps (including co-registration and concatenation of the three FMISO PET/CT scans, tumor segmentation, input function definition and partial-volume correction, and calculation of parametric maps via voxelwise kinetic modeling) can in principle be largely automated.

Conclusion

Pharmacokinetic modeling of FMISO dPET allows for simultaneous multiparametric imaging of tumor hypoxia and perfusion, as well as FMISO distribution volume. These data can clarify the ambiguity in interpreting the late static FMISO exams and improve the characterization of hypoxic subregions for e.g. therapy planning, patient stratification or response assessment. Our demonstration of the feasibility to obtain equivalent k_3 and K_1 data based on the utilization of 20-min acquisitions increases the practicality of performing FMISO dynamic PET exams within a busy clinical department.

References

1. Rajendran JG, Schwartz DL, O'Sullivan J, et al. Tumor hypoxia imaging with [F-18]fluoromisonidazole positron emission tomography in head and neck cancer. *Clin Cancer Res* 2006;12:5435-5441.

2. Wilson WR, Hay MP, Targeting hypoxia in cancer therapy. *Nat Rev Cancer* 2011;11:393-410.

3. Jain RK. Antiangiogenesis strategies revisited: from starving tumors to alleviating hypoxia. *Cancer Cell* 2014;26:605-622.

4. Carmeliet P, Jain RK. Molecular mechanisms and clinical applications of angiogenesis. *Nature* 2011;473:298-307.

5. Yang MH, Wu MZ, Chiou SH, et al. Direct regulation of TWIST by HIF-1alpha promotes metastasis. *Nat Cell Biol* 2008;10:295-305.

6. Brizel DM, Sibley GS, Prosnitz LR, Scher RL, Dewhirst MW. Tumor hypoxia adversely affects the prognosis of carcinoma of the head and neck. *Int J Radiat Oncol Biol Phys* 1997;38:285-289.

7. Horsman MR, Mortensen LS, Petersen JB, Busk M, Overgaard J. Imaging hypoxia to improve radiotherapy outcome. *Nat Rev Clin Oncol* 2012;9:674-687.

8. Koh WJ, Rasey JS, Evans ML, et al. Imaging of hypoxia in human tumors with [F-18]fluoromisonidazole. *Int J Radiat Oncol Biol Phys* 1992;22:199-212.

9. Rasey JS, Koh WJ, Evans ML, et al. Quantifying regional hypoxia in human tumors with positron emission tomography of [18F]fluoromisonidazole: a pretherapy study of 37 patients. *Int J Radiat Oncol Biol Phys* 1996;36:417-428.

10. Okamoto S, Shiga T, Yasuda K, et al. High reproducibility of tumor hypoxia evaluated by 18F-fluoromisonidazole PET for head and neck cancer. *J Nucl Med* 2013;54:201-207.

11. Grkovski M, Schwartz J, Rimner A, et al. Reproducibility of 18F-fluoromisonidazole intratumour distribution in non-small cell lung cancer. *EJNMMI Res* 2016;6:79.

12. Rischin D, Hicks RJ, Fisher R, et al. Prognostic significance of [18F]-misonidazole positron emission tomography-detected tumor hypoxia in patients with advanced head and neck cancer randomly assigned to chemoradiation with or without tirapazamine: a substudy of Trans-Tasman Radiation Oncology Group Study 98.02. *J Clin Oncol* 2006;24:2098-2104.

13. Rajendran JG, Krohn KA. F-18 fluoromisonidazole for imaging tumor hypoxia: imaging the microenvironment for personalized cancer therapy. *Semin Nucl Med* 2015;45:151-162.

14. Patlak CS, Blasberg RG. Graphical evaluation of blood-to-brain transfer constants from multiple-time uptake data. Generalizations. *J Cereb Blood Flow Metab* 1985;5:584-590.

15. Koch CJ, Evans SM. Optimizing hypoxia detection and treatment strategies. *Semin Nucl Med* 2015;45:163-176.

16. Bruehlmeier M, Roelcke U, Schubiger PA, Ametamey SM. Assessment of hypoxia and perfusion in human brain tumors using PET with 18F-fluoromisonidazole and 15O-H2O. *J Nucl Med* 2004;45:1851-1859.

17. Padhani AR, Miles KA. Multiparametric imaging of tumor response to therapy. *Radiology* 2010;2:348-364.

18. Kadrmas DJ, Hoffman JM. Methodology for quantitative rapid multi-tracer PET tumor characterizations. *Theranostics* 2013;3:757-773.

19. Dunnwald LK, Gralow JR, Ellis GK, et al. Tumor metabolism and blood flow changes by positron emission tomography: relation to survival in patients treated with neoadjuvant chemotherapy for locally advanced breast cancer. *J Clin Oncol* 2008;26:4449-4457.

20. Komar G, Kauhanen S, Liukko K, et al. Decreased blood flow with increased metabolic activity: a novel sign of pancreatic tumor aggressiveness. *Clin Cancer Res* 2009;15:5511-5517.

21. Yankeelov TE, Abramson RG, Quarles CC. Quantitative multimodality imaging in cancer research and therapy. *Nat Rev Clin Oncol* 2014 ;11:670-680.

22. Eschmann SM, Paulsen F, Reimold M, et al. Prognostic impact of hypoxia imaging with 18F-misonidazole PET in non-small cell lung cancer and head and neck cancer before radiotherapy. *J Nucl Med* 2005;46:253-260.

23. Thorwarth D, Eschmann SM, Scheiderbauer J, Paulsen F, Alber M. Kinetic analysis of dynamic 18F-fluoromisonidazole PET correlates with radiation treatment outcome in head-and-neck cancer. *BMC Cancer* 2005;5:152.

24. Dunnwald LK, Doot RK, Specht JM, et al. PET tumor metabolism in locally advanced breast cancer patients undergoing neoadjuvant chemotherapy: value of static versus kinetic measures of fluorodeoxyglucose uptake. *Clin Cancer Res* 2011;17:2400-2409.

25. Ang KK, Harris J, Wheeler R, et al. Human papillomavirus and survival of patients with oropharyngeal cancer. *N Engl J Med* 2010;363:24-35.

26. Lim JL, Berridge MS. An efficient radiosynthesis of [18F]fluoromisonidazole. *Appl Radiat Isot* 1993;44:1085–1091.

27. Grkovski M, Schwartz J, Gönen M, et al. Feasibility of 18F-Fluoromisonidazole Kinetic Modeling in Head and Neck Cancer Using Shortened Acquisition Times. *J Nucl Med* 2016;57:334-341.

28. Rajendran JG, Mankoff DA. Positron Emission Tomography Imaging of Blood Flow and Hypoxia in Tumors. In Shields, AF., Price P. In vivo imaging of cancer therapy. Springer Science & Business Media, 2007.

29. Mankoff DA, Dunnwald LK, Partridge SC, Specht JM. Blood flow-metabolism mismatch: good for the tumor, bad for the patient. *Clin Cancer Res* 2009;15:5294-5296

30. Mankoff DA, Dunnwald LK, Gralow JR, et al. Blood flow and metabolism in locally advanced breast cancer: relationship to response to therapy. *J Nucl Med* 2002 (4):500-509.

31. Lehtiö K, Eskola O, Viljanen T, et al. H. Imaging perfusion and hypoxia with PET to predict radiotherapy response in head-and-neck cancer. *Int J Radiat Oncol Biol Phys* 2004;59:971-982.

32. Lehtiö K, Oikonen V, Grönroos T, et al. Imaging of blood flow and hypoxia in head and neck cancer: initial evaluation with [(15)O]H(2)O and [(18)F]fluoroerythronitroimidazole PET. *J Nucl Med* 2001;42:1643-1652.

33. Ljungkvist AS, Bussink J, Rijken PF, Kaanders JH, van der Kogel AJ, Denekamp J. Vascular architecture, hypoxia, and proliferation in first-generation xenografts of human head-and-neck squamous cell carcinomas. *Int J Radiat Oncol Biol Phys* 2002;54:215-228.

34. Dewhirst MW, Navia IC, Brizel DM, Willett C, Secomb TW. Multiple etiologies of tumor hypoxia require multifaceted solutions. *Clin Cancer Res* 2007;13:375-377.

35. Komar G, Seppänen M, Eskola O, et al. 18F-EF5: a new PET tracer for imaging hypoxia in head and neck cancer. *J Nucl Med* 2008;49:1944-1951.

Table 1. Subject demographics and clinical characteristics

Characteristics	N=120 (%)
Gender	
Male	108 (90)
Female	12 (10)
Age at diagnosis, y	
<40	1 (1)
40-49	19 (16)
50-59	46 (38)
60-69	37 (31)
70-79	12 (10)
80+	5 (4)
Clinical tumor classification	
T1	30 (25)
T2	52 (43)
T3	17 (14)
T4	13 (11)
Unknown	8 (7)
Tumor subsite	
Base of tongue	54 (45)
Tonsil	53 (44)
Hypopharynx	2 (2)
Supraglottic larynx	3 (2)
Unknown primary	8 (7)
Clinical lymph node classification	
N0	1 (1)*
N1	15 (12)
N2a	14 (11)
N2b	50 (42)
N2c	37 (31)
N3	2 (27)
Unknown	1 (1)
HPV status†	
Positive	73 (83)
Negative	15 (17)
Testing not performed	32
p16 status†	
Positive	96 (91)
Negative	9 (9)
Testing not performed	15

*Numbers do not total 100% due to rounding. †Both HPV and p16 information was available for n=77 patients. 8 patients were HPV-negative and p16-negative, 5 patients were HPV-negative while being p16-positive, and 64 patients were HPV-positive and p16-positive.

Table 2. Summary of investigated metrics for all analyzed tissues.

Tissue	Target-to-blood Ratio	k_3 (min^{-1})	K_1 (min^{-1})	K_1/k_2	v_B	Distribution volume	Equilibration time (min)
Lesion (Mean intratumor)	1.30±0.30	0.0027± 0.0021	0.35±0.17	0.96± 0.17	0.19± 0.10	0.95±0.14	15±6
Lesion (Voxelwise)	1.45±0.48	0.0036± 0.0035	0.33±0.19	0.97± 0.22	0.19± 0.12	0.96±0.18	18±5
SCM muscle	1.02±0.06	0.0008± 0.0006	0.08±0.04	0.89± 0.09	0.05± 0.03	0.90±0.08	73±45
Adipose tissue	0.28±0.07	0.0004± 0.0004	0.02±0.01	0.24± 0.06	0.01± 0.01	0.25±0.06	67±38
Submandibular gland	1.04±0.08	0.0002± 0.0004	0.64±0.41	1.05± 0.12	0.14± 0.09	1.04±0.10	10±5
Parotid gland	0.92±0.11	0.0002± 0.0004	0.50±0.38	0.89± 0.14	0.10±. 07	0.90±0.13	13±9

Table 3. Reproducibility of kinetic rate constants using 20-min truncated dataset*.

Kinetic rate constant	Tumor level (n=248)					Voxel level			
	r	Slope (95% CI)	Intercept (95% CI)	RMSD	Mean difference (95% LoA)	*r*	Slope	Intercept	Mean difference (95% LoA)
k_3 (min^{-1})	0.98	1.000 (0.977 to 1.003)	3E-5 (-6E-5 to 1E4)	0.0005± 0.0004	3.5E-5 (-0.0008 to 0.0009)	0.98	1.034	-9E-6	1.1E-4 (-0.0015 to 0.0017)
K_1 (min^{-1})	1.00	0.966 (0.955 to 0.977)	0.016 (0.012 to 0.020)	0.017± 0.010	0.004 (-0.024 to 0.033)	0.99	0.971	0.017	0.007 (-0.042 to 0.057)
K_1/k_2	0.98	1.073 (1.045 to 1.100)	-0.08 (-0.11 to -0.06	0.06± 0.03	-0.02 (-0.09 to 0.06)	0.96	1.064	-0.08	-0.02 (-0.16 to 0.12)
v_B	0.99	0.992 (0.977 to 1.007)	-3E-3 (-6E-3 to 2E-8)	0.01± 0.01	-0.004 (-0.026 to 0.017)	0.98	0.977	-4E-4	-0.005 (-0.045 to 0.036)
DV	0.98	1.088 (1.060 to 1.115)	-0.10 (-0.12 to -0.07)	0.04± 0.02	-0.01 (-0.08 to 0.05)	0.96	1.073	-0.09	-0.02 (-0.13 to 0.09)

*0-10 min dynamic + 10 min static acquisition starting at 160 min post-injection (20-min total acquisition time).

Table 4. Reproducibility of kinetic rate constants using 15-min truncated dataset*.

Kinetic rate constant	Tumor level (n=248)					Voxel level			
	r	Slope (95% CI)	Intercept (95% CI)	RMSD	Mean difference (95% LoA)	*r*	Slope	Intercept	Mean difference (95% LoA)
k_3 (min^{-1})	0.95	1.057 (1.010 to 1.103)	7E-5 (-9E-5 to 2E4)	0.0011± 0.0009	0.0002 (-0.0014 to 0.0015)	0.91	1.070	5E-5	0.0003 (-0.0032 to 0.0037)
K_1 (min^{-1})	0.99	0.948 (0.931 to 0.965)	0.033 (0.026 to 0.040)	0.035± 0.018	0.015 (-0.029 to 0.058)	0.98	0.962	0.031	0.019 (-0.065 to 0.102)
K_1/k_2	0.92	1.089 (1.025 to 1.154)	-0.11 (-0.18 to -0.05	0.14± 0.06	-0.03 (-0.18 to 0.12)	0.81	1.072	-0.11	-0.04 (-0.37 to 0.29)
v_B	0.99	0.981 (0.958 to 1.004)	-5E-3 (-9E-3 -to 3E-3)	0.02± 0.01	-0.008 (-0.039 to 0.022)	0.97	0.970	-3E-3	-0.009 (-0.061 to 0.043)
DV	0.93	1.124 (1.059 to 1.188)	-0.15 (-0.21 to -0.08)	0.12± 0.05	-0.03 (-0.16 to 0.10)	0.82	1.095	-0.13	-0.04 (-0.30 to 0.22)

*0-5 min dynamic + 10 min static acquisition starting at 160 min post-injection (15-min total acquisition time).

FIGURES

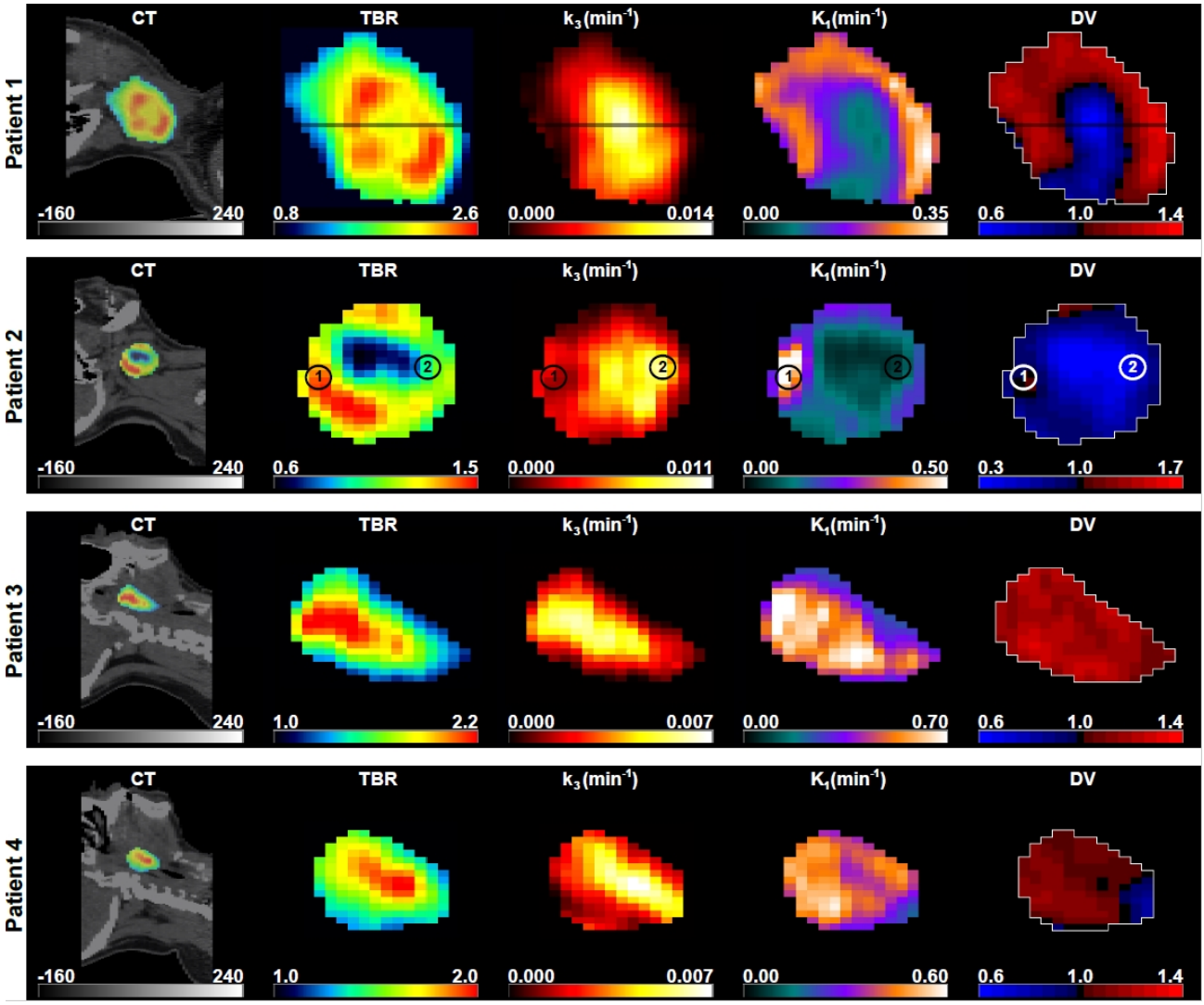

Figure 1. Sagittal images of 4 representative patients: From left to right: the late 10-min FMISO PET/CT scan, target-to-blood ratio (*TBR*), k_3 map representing hypoxia-mediated entrapment of FMISO, K_1 map, a surrogate measure of perfusion, and FMISO distribution volume (*DV*), representing overall concentration of unbound FMISO relative to blood. Window levels are set according to the scale bars and are adjusted for maximum visibility.

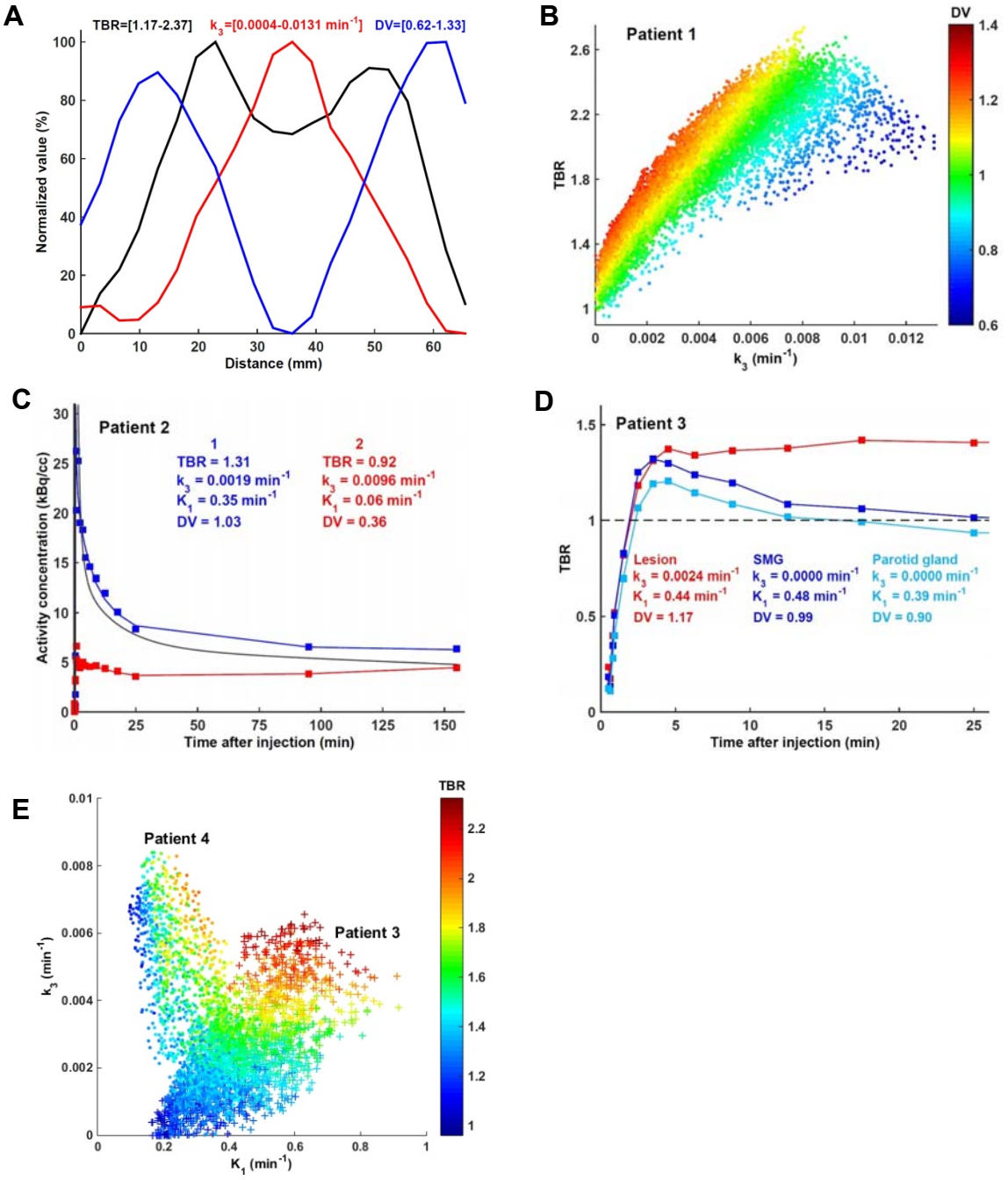

Figure 2. (A) Line profile through *TBR*, k_3 and *DV* parametric maps for Patient #1 from Fig. 1 with HPV-negative, p16-positive T1N2c tumor originating in the base of tongue. The minimum and maximum values of each parameter are normalized between 0-100% corresponding to the actual parameter values provided in brackets in the top of the figure. (B) k_3-*TBR* voxelwise scatterplot for Patient #1, color-coded according to the *DV*. (C) Modeled time activity curves (solid line) superimposed on measured time activity curves (squares) from two voxels in hyperperfused and relatively normoxic (area 1 on Fig. 1; blue) and

hypoperfused and hypoxic tumor subregions (area 2 on Fig 1; red) for Patient #2 with HPV-positive, p16-positive T1N2a tumor originating in the tonsil. The parameter values for each voxel are given in the top of the Figure. Also displayed is the time activity curve for the input function (black). (D) Target-to-blood ratio as a function of time after injection is shown for Patient #3 with HPV-positive, p16-positive T2N2b tumor originating in the tonsil, whose lesion exhibited uniformly high distribution volume (*DV*=1.17). Also included are corresponding data for normoxic submandibular (SMG) and parotid glands. (E) Scatterplot of perfusion (K_1) and hypoxia (k_3) parameters for Patient #3 (crosses; HPV-positive, p16-positive T2N2b tumor originating in the tonsil) and Patient #4 (dots; HPV-positive, p16-positive T3N1 tumor originating in the tonsil), exhibiting a positive (Pearson's r =0.71) and negative (Pearson's r = -0.61) trend between K_1-k_3, respectively.

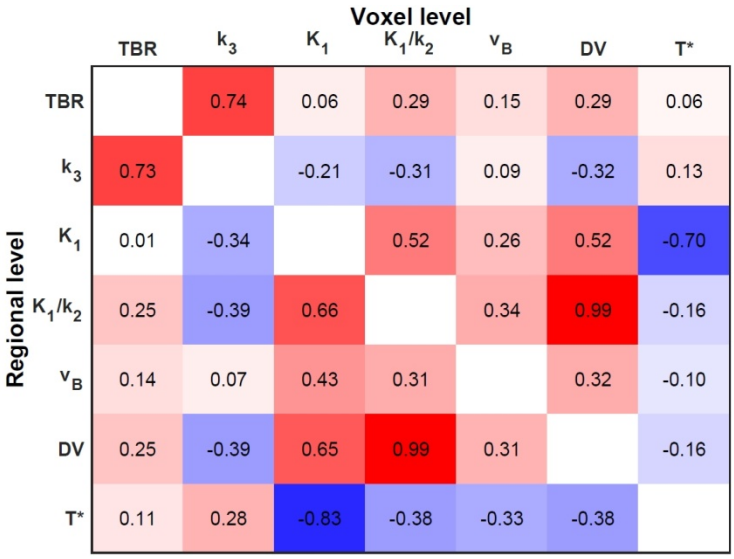

Figure 3. Correlation matrix of Pearson correlation between all investigated parameters. The upper right and lower left triangles shows coefficients derived on the voxel and regional level, respectively.

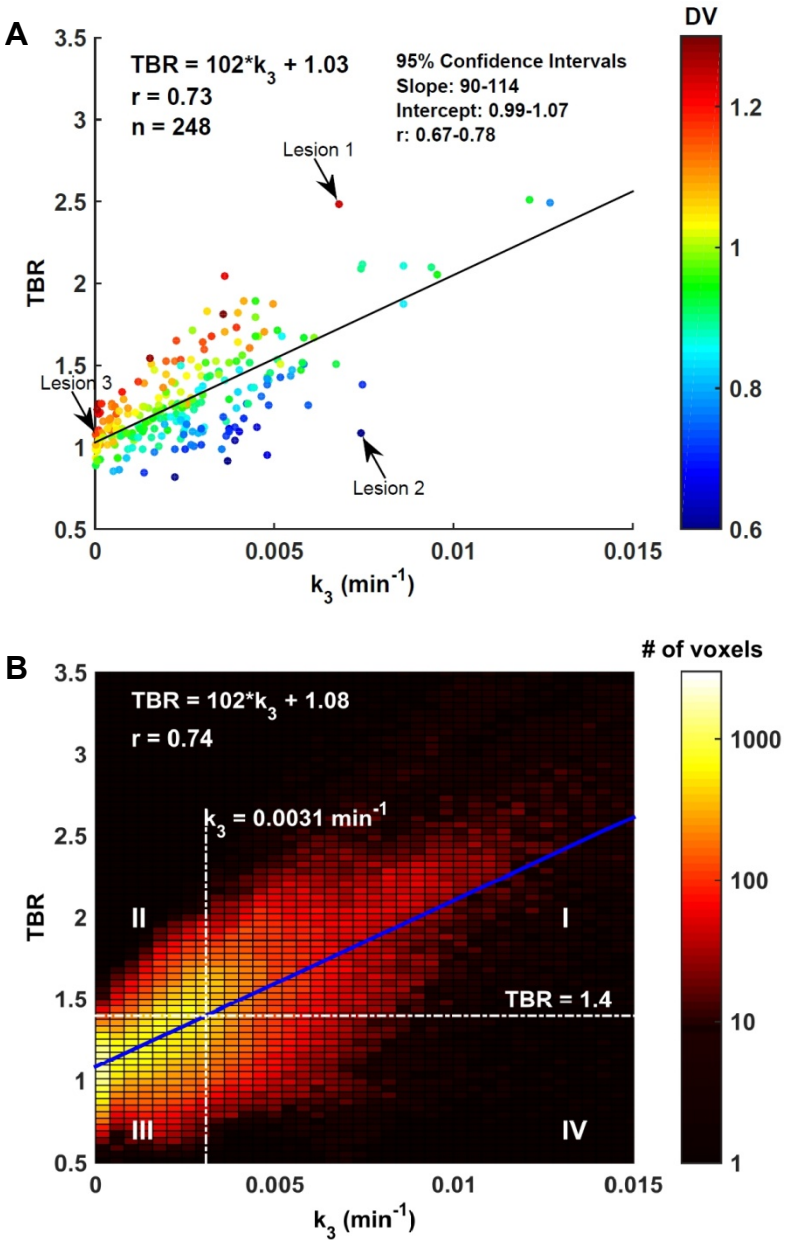

Figure 4. (A) Scatterplot of mean intratumor k_3 and *TBR* for all analyzed lesions, color-coded according to mean intratumor *DV*. (B) Corresponding k_3-*TBR* intensity histogram for voxelwise values from pooled data. Included are nominal hypoxia thresholds based on *TBR* = 1.4 and regression-derived k_3 = 0.0031 min^{-1}.

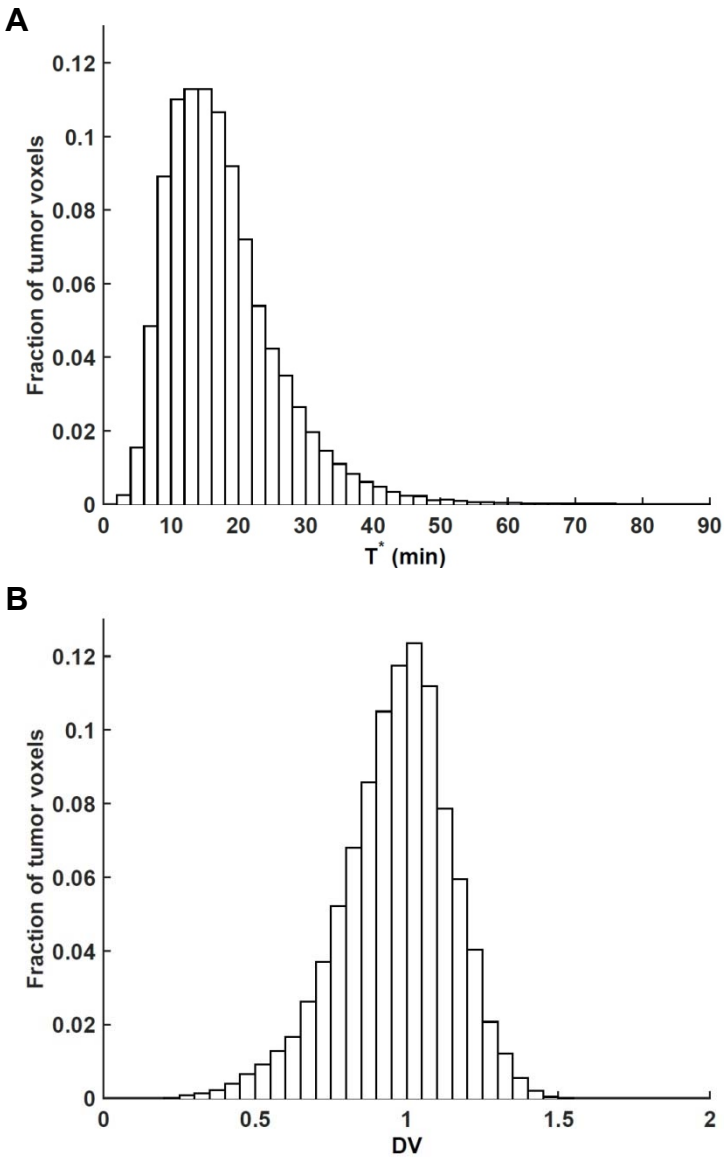

Figure 5. (A) Frequency histogram of (A) FMISO equilibration time *T** and (B) FMISO distribution volume *DV* for pooled voxelwise data.

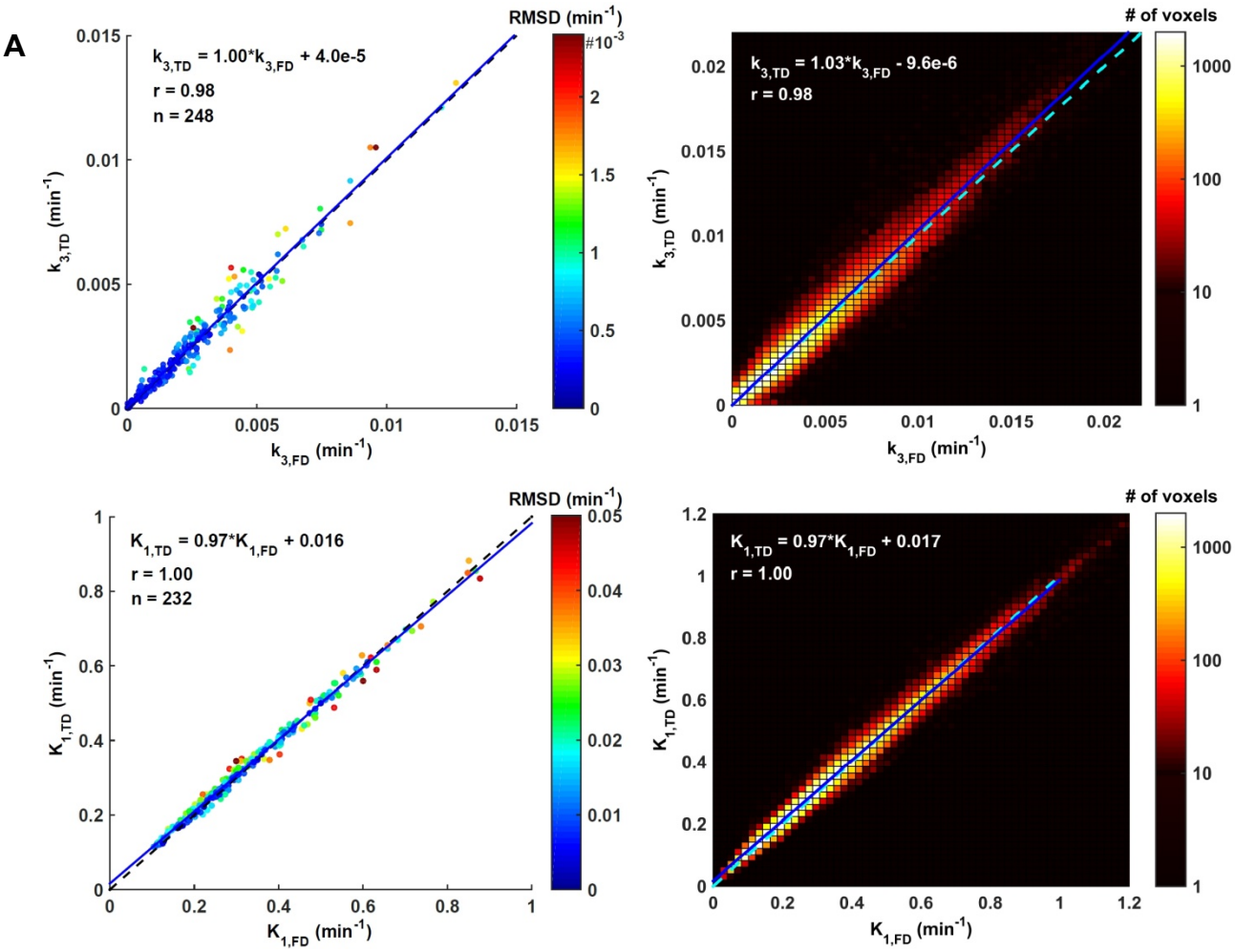
A
RMSD (min-1)
#10-3
k3,TD = 1.00*k3,FD + 4.0e-5
r = 0.98
n = 248
k3,TD (min-1)
k3,FD (min-1)
# of voxels
k3,TD = 1.03*k3,FD - 9.6e-6
r = 0.98
K1,TD = 0.97*K1,FD + 0.016
r = 1.00
n = 232
K1,TD (min-1)
K1,FD (min-1)
K1,TD = 0.97*K1,FD + 0.017
r = 1.00

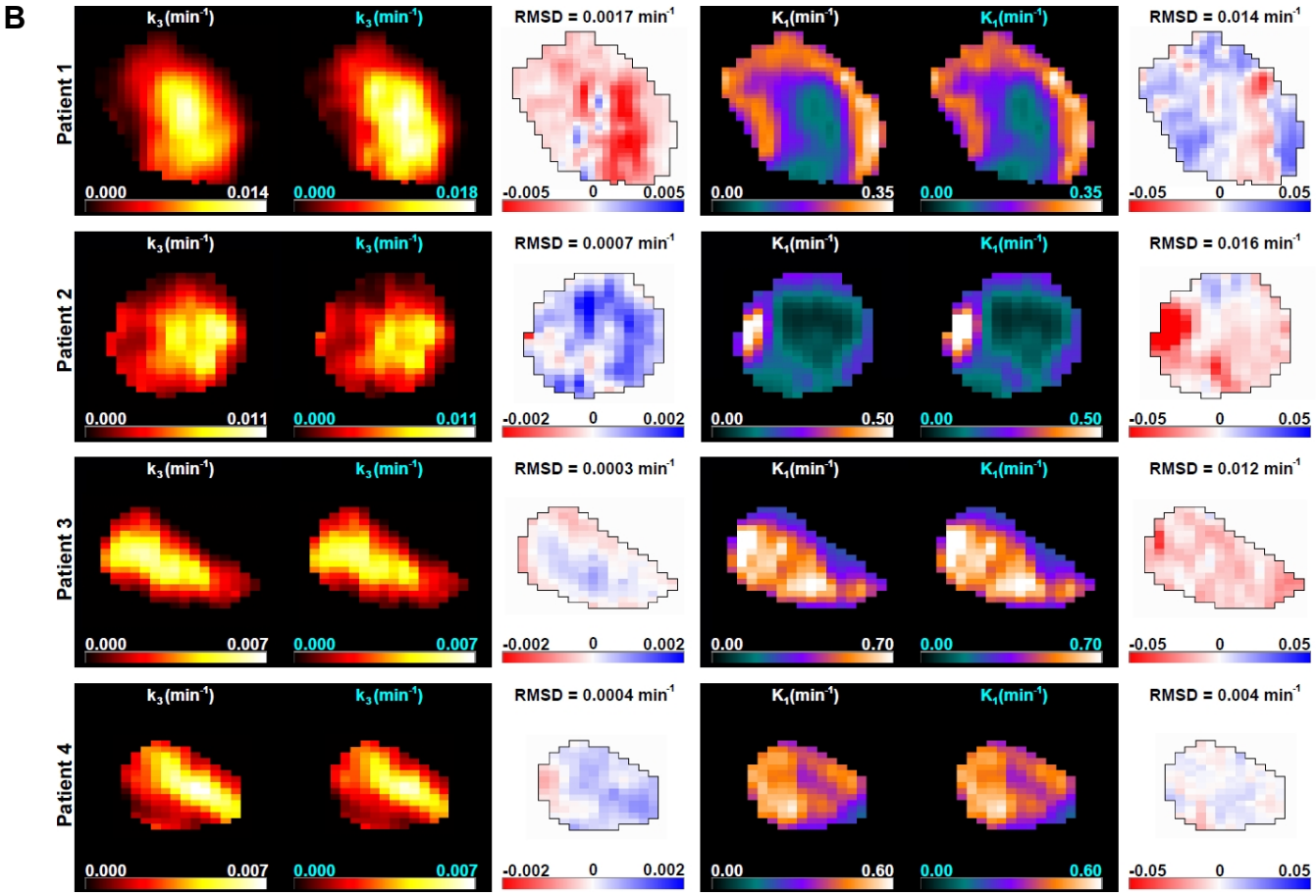

Figure 6. (A) Left column: scatterplot of average intratumor k_3 (top) and K_1 (bottom) for the full dataset (FD; abscissa) versus truncated 20-min dataset (TD; ordinate), color color-coded according to root-mean-square deviation (RMSD) of residuals. Right column: Corresponding intensity histograms of voxelwise k_3 (top) and K_1 (bottom) values from pooled data. Identity (dashed) and regression (solid) lines are superimposed in all foregoing cases. (B) From left to right: k_3 parametric maps as calculated with FD and TD, k_3 difference map (i.e. k_3(FD) - k_3(TD)), and equivalent maps for K_1, for all patient example tumors shown in Figure 1.